

Copyright
by
Elizabeth Anne Vokac
2011

**The Thesis Committee for Elizabeth Anne Vokac
Certifies that this is the approved version of the following thesis:**

**Localized Surface Plasmon Resonance Spectroscopy of Gold and Silver
Nanoparticles and Plasmon Enhanced Fluorescence**

**APPROVED BY
SUPERVISING COMMITTEE:**

Supervisor:

Katherine A. Willets

Jennifer S. Brodbelt

**Localized Surface Plasmon Resonance Spectroscopy of Gold and Silver
Nanoparticles and Plasmon Enhanced Fluorescence**

by

Elizabeth Anne Vokac, B.S.; B.S.

Thesis

Presented to the Faculty of the Graduate School of

The University of Texas at Austin

in Partial Fulfillment

of the Requirements

for the Degree of

Master of Arts

The University of Texas at Austin

December, 2011

Dedication

This thesis is dedicated to all of my family and friends, and especially to my parents.

Acknowledgements

First, I would like to express my gratitude to my supervisor, Professor Katherine Willets, for taking me into her lab and for her support and guidance. I would also like to thank my entire research group for their warmth and advice and especially Kathryn Mayer and Katherine Koen for their knowledge and patience. I am grateful to my committee member Jennifer S. Brodbelt for her time spent on counseling my thesis.

In addition, I would like to thank my parents Lucy Vokac and Thomas Vokac, my aunt and uncle Judy Vokac and James Vokac, my grandfather Salvatore Vasile and my best friend Justin Main for their endless love and support throughout my absence.

Abstract

Localized Surface Plasmon Resonance Spectroscopy of Gold and Silver Nanoparticles and Plasmon Enhanced Fluorescence

Elizabeth Anne Vokac, M.A.

The University of Texas at Austin, 2011

Supervisor: Katherine Willets

This thesis presents spectroscopic studies of metallic nanoparticle localized surface plasmons and plasmon enhanced fluorescence. We investigated the dielectric sensitivity of silver nanoprisms to an external electric field and gold nanorods to the formation of a self-assembled surface monolayer. Dark field microscopy was used to image plasmonic scattering from single nanoparticles, and a liquid crystal tunable filter was used to construct corresponding spectra. The plasmon resonances of silver nanoprisms displayed both reversible red shifts and irreversible blue shifts along with drastic intensity changes upon exposure to an applied bias. The plasmon resonances of gold nanorods showed sensitivity to the presence of alkanethiol molecules adhered to the particle surface by a moderate red shift. An increase in the effective external dielectric caused a shift toward longer wavelengths.

We imaged plasmon enhanced fluorescence in order to optimize experimental parameters for a developing project that can characterize nanoparticle structure on sub-wavelength dimensions. Preliminary controls were performed to account for the effect of

O₂ plasma treatment, solvent and alkanethiol monolayer formation on surface plasmon resonances. We found that O₂ plasma treatment for different time intervals did not result in a plasmon shift compared to untreated nanoparticles exposed to N₂; however when exposed to solvent the surface plasmons of the treated particles shifted five times as far toward the red. Interestingly, the solvent effect only resulted in a plasmon shift when the particles were N₂ dried after solvent incubation. Gold nanorods incubated in ethanol showed no wavelength maximum shift in pure solvent over time, but shifted moderately to the red after incubation in a solution of alkanethiol molecules. Conditions for the plasmon enhanced fluorescence study were optimized using a dye conjugate of the same alkanethiol molecule used previously by formation from solution in a monolayer on the gold nanorod surface. The appropriate synthesis for dye functionalization, molecular concentrations, solvents and optical settings were determined.

Table of Contents

Chapter 1: Introduction.....	1
Chapter 2: Experimental.....	6
2.1 POTENTIAL INDUCED LSPR SHIFT OF SILVER NANOPRISMS ...	6
2.1.1 Materials	6
2.1.2 Sample preparation	6
2.2 SAM INDUCED LSPR SHIFT OF GOLD NANORODS.....	8
2.2.1 Materials	8
2.2.2 Sample preparation	8
2.3 DARK FIELD MICROSCOPY EXPERIMENTAL SET UP.....	9
2.4 LSPR SPECTROSCOPY DATA COLLECTION	10
2.4.1 Single nanoparticle confirmation.....	11
Chapter 3: Dielectric Sensitivity of Silver Nanoprisms.....	13
3.1 INTRODUCTION	13
3.2 ELECTRIC POTENTIAL INDUCED SHIFT OF LSPR.....	13
3.2.1 Measurement technique and experimental set up	13
3.2.2 Results and discussion	15
3.3 CONCLUSION.....	20
Chapter 4: LSPR Sensitivity to a Self-Assembled Monolayer and Plasmon Enhanced Fluorescence	21
4.1 INTRODUCTION	21
4.2 EXPERIMENTAL.....	22
4.2.1 Materials	22
4.2.2 Synthesis of dye functionalized SAM molecule.....	22
4.2.3 Fluorescence experimental set up	24
4.2.4 Grazing angle reflection absorption infrared spectroscopy	25
4.3 DARK FIELD IMAGES AND LSPR SPECTRA.....	26
4.4 SAM INDUCED LSPR SHIFT	27
4.4.1 Measurement techniques.....	28

4.4.2 Discussion	29
4.5 DYE FUNCTIONALIZED SAM FLUORESCENCE	35
4.5.1 Grazing Angle Reflection Absorption Infrared Spectroscopy analysis	35
4.5.2 TAMRA-MUAM diffusion and SAM formation on Au NRs	40
4.5.3 TAMRA-MUAM fluorescence.....	41
Chapter 5: Conclusion and Future Work	45
5.1 CONCLUSION.....	45
5.2 FUTURE WORK.....	46
References.....	47

Chapter 1: Introduction

The utility of plasmonic nanostructures has branched into a multitude of disciplines and still new applications continue to emerge. Their unique properties are exploited in tools such as opto-electronic devices, fuel cells, bio-imaging and photothermal therapy.¹⁻⁴ Noble metal nanoparticles are heavily employed as optical sensors due to their capability of highly sensitive, non-destructive detection. Radiation enhancement at the metallic surface via electromagnetic (EM) coupling between excitation light and electronic excitations makes these particles suitable for surface-enhanced spectroscopy. Ensemble studies of nanoparticles provide limited information about the relationship between structure and enhancement due to the heterogeneity of sample populations as a result of current synthesis and fabrication techniques. Single nanoparticle studies are necessary to characterize the relationship between particle structure and field enhancement. In order for plasmonic nanoparticles to be of maximal use, characterization and control over their surface plasmon response must be achieved.

The localized surface plasmon resonance (LSPR) is defined as the radiation (or light)-driven collective oscillation of the surface conduction electrons in a noble metal nanostructure. The interaction of spherical plasmonic materials and EM radiation within the limitations of the nanoscale regime can be approximated using Maxwell's equations. The EM field external to a spherical nanostructure with a radius smaller than the wavelength of light ($a < \lambda$) can be shown by the following equation.^{5,6}

$$E_{out}(x, y, z) = E_0 \hat{z} - \left[\frac{\epsilon_{in} - \epsilon_{out}}{(\epsilon_{in} + 2\epsilon_{out})} \right] a^3 E_0 \left[\frac{\hat{z}}{r^3} - \frac{3z}{r^5} (x \hat{x} + y \hat{y} + z \hat{z}) \right] \quad (1)$$

Here, E_0 is the incident EM field, ϵ_{in} is the wavelength dependent dielectric function of the metal, ϵ_{out} is the dielectric function of the surroundings, z is the light polarization direction and r is the distance from the sphere surface. A dielectric resonance condition is met when $\epsilon_{in} \approx -2\epsilon_{out}$ resulting in great EM enhancement at the nanoparticle surface. For gold and silver, this resonance condition falls in the visible region of the spectrum making these materials useful for a broad range of applications.

The total amount of light that is elastically scattered and absorbed by the nanoparticle is known as the extinction. The wavelength dependent extinction spectrum for a metal sphere is represented by the following equation.^{7, 8}

$$E(\lambda) = \frac{24\pi^2 N a^3 \epsilon_{out}^{\frac{3}{2}}}{\lambda \ln(10)} \left[\frac{\epsilon_i(\lambda)}{(\epsilon_r(\lambda) + \chi \epsilon_{out})^2 + \epsilon_i(\lambda)^2} \right] \quad (2)$$

Here N is the number of combined polarizable elements used to represent the particle, ϵ_i is the imaginary dielectric component of the metal, ϵ_r is the real dielectric component of the metal, χ is a geometric factor approximated for all shapes other than spheres and all other parameters are as defined above. In order for a material to be plasmonic, it must possess a negative real and small positive imaginary dielectric function. In addition to the LSPR wavelength maximum (λ_{MAX}) dependence on the internal dielectric of the metal, it is sensitive to particle size, shape and external dielectric. Particles of the same size and material, but different shape, will not have the same LSPR extinction spectrum. Similarly, identical particles exposed to environments with different refractive indices ($\epsilon = n^2$) will also have different LSPR spectra. Because the effects of particle shape and size have been investigated extensively^{9, 10}, here the focus is on the nanoparticle LSPR response to a change in the external dielectric.

In this study we explored the sensitivity of plasmonic nanoparticles to the external dielectric by both exposure to an electric potential and surface modification with a molecular monolayer. When an external electric potential is applied across plasmonic nanoparticles, the electron density is modulated, causing the LSPR λ_{MAX} to shift.¹¹ In a study by Zhang et al. the LSPR shift of plasmonic nanoparticle arrays was controlled using an applied electric field. The authors quantitatively calibrated their system in air ($\epsilon \approx 1.00$) by applying a potential across Au nanodisks on a conductive substrate and measuring the change in scattering signal as the voltage was increased. To explain changes in scattering signal in terms of a voltage induced resonance wavelength shift the authors empirically derived equation 3 below.¹¹

$$\Delta\lambda = -\frac{\epsilon_0 \omega_p^{*2} \lambda^3}{8\pi^2 c^2 N e d_{TF} \left(\epsilon_\infty + \frac{1-L}{L}\right)} \frac{V_0}{d} \quad (3)$$

Here ϵ_0 is the vacuum permittivity (constant), ω_p is the plasma frequency of the bulk metal, λ is LSP wavelength, N is the metal electron density, d_{TF} is the Thomas-Fermi screening length (constant), ϵ_∞ is the high frequency dielectric, L is a depolarization shape factor, d is the distance between the electrodes and V_0 is the applied voltage. The properties characteristic to silver metal in the above equation (plasma frequency of Ag ($\omega_p \approx 9.04$ eV, 1.37 E^{16} Hz)^{12, 13} and the LSP wavelength ($\lambda_{\text{LSP}} \approx 670$ nm)¹⁴ were used to estimate the amount of voltage required to observe a measurable shift in the plasmon ($\Delta\lambda_{\text{LSPR}}$) of our Ag nanoprisms and found to be ca. 600 V.

Another means by which the LSPR can be modulated is by the formation of a self-assembled monolayer (SAM) on the particle surface. The adhered molecules alter the local environment by a change in effective refractive index, commonly used in

sensing applications.¹⁵ The impact of a change in external dielectric increases with proximity to the nanostructure surface, making this a very sensitive effect.¹⁶ The following equation describes the relationship between effective refractive index change and LSPR wavelength maximum shift.^{17, 18}

$$\Delta\lambda_{max} = m\Delta n \left[1 - \exp\left(\frac{-2d}{l_d}\right) \right] \quad (4)$$

Here m is the bulk refractive index response, Δn is the monolayer induced change in refractive index, d is the monolayer thickness and l_d is the decay length of the EM field. In addition to the detection of SAM surface modification by LSPR sensing, fluorescence from a dye-functionalized SAM molecule during monolayer formation can be imaged. The observation of plasmon enhanced fluorescence can help to verify the formation of a SAM of dye-functionalized molecules on a plasmonic nanoparticle surface and provide information about nanoparticle structure and location. This imaging technique is a powerful way to uncover nanostructure information masked by the diffraction limit of light.

The challenges in optical measurements of nanoparticles are a direct result of the small particle size. Light scattered from any object smaller than ca. half the wavelength of light is diffraction limited, leading to image expansion and distortion.¹⁹ The Abbe diffraction limit describes the spot size dimensions for objects smaller than the wavelength of light (λ) imaged under a microscope. In equation 5 shown here,

$$d = \frac{\lambda}{2(n \sin\theta)} \quad (5)$$

d is the radius of the spot size to which light will converge, n is the refractive index of imaging media and θ is half the angle spanned by the lens. When imaging an object with white light (ca. 400 nm – 700 nm) the smallest object that will not be diffraction limited is ca. half the wavelength of the longer end of the range (700 nm). This will distort the image of any object smaller than 350 nm, which is over three times larger than the 100 nm particles we studied.

Plasmonic nanoparticles have an enormous scattering cross section resulting in a strong signal. Yet, overwhelming excitation light must be rejected to successfully detect the relatively much weaker scattering signal. Dark field microscopy is a widely used technique for imaging plasmonic nanoparticles by Rayleigh (elastic) light scattering because of its ability to address this issue.

In this body of work we used dark field microscopy to image plasmonic metal nanostructures. We investigated the shift in LSPR wavelength maximum ($\Delta\lambda_{\max}$) of Ag and Au nanoparticles due to changes in their external environment. The change in plasmon extinction was studied for Ag nanoprisms embedded in crystalline SiO₂ and exposed to an external electric field and for Au nanorods (NRs) modified with a SAM on the particle surface. Experimental parameter optimization for a future plasmon enhanced fluorescence study was done.

Chapter 2: Experimental

2.1 POTENTIAL INDUCED LSPR SHIFT OF SILVER NANOPRISMS

2.1.1 Materials

Photrex grade wash solvent materials, 99.8 % ethanol, 99.9 % acetone and 100 % isopropanol were purchased from JT Baker. Nitric acid (70%) was purchased from Aldrich and diluted to 7 %. ITO patterned glass slides (22 x 22 x 1 mm, resistivity ca. 60 Ω /sq, transmission ca. 87%) were purchased from Evaporated Coatings. High purity aluminum for deposition was purchased from Ted Pella. Thin tungsten wire and tungsten and molybdenum deposition boats were purchased from the physics department storeroom at the University of Texas. Conductive epoxy was purchased from HMC Electronics. Details of the SiO₂ layer are below in 2.1.2. Silver nanoprisms were synthesized with sodium citrate, silver nitrate, sodium borohydride (NaBH₄) and bis(*p*-sulfonatophenyl)phenylphosphine (BSPP), purchased from Sigma-Aldrich.

2.1.2 Sample preparation

All samples for this experiment were made on 22 mm² glass slides patterned with four ITO electrode sites. The slides were cleaned by sonication for 10 minutes each in ethanol, acetone and isopropanol. A 200 nm layer of SiO₂ ($n = 1.46$ at 632.8 nm, $\epsilon \approx 4.4$)^{20, 21} was deposited on the ITO by inductively-coupled plasma - plasma enhanced chemical vapor deposition (ICP-PECVD) in an Oxford Systems chamber (Oxford Plasmalab80plus). The sample was heated to 200°C in a vacuum chamber at 1 mtorr where gaseous sources of SiH₄ and N₂O were then flowed in while a 13.56 MHz parallel plate reactor created a plasma density of ca. $5 \times 10^{11}/\text{cm}^2$. Reactant gas ions were driven

by the radio frequency (RF) forward power to create a very high quality SiO₂ film. After deposition, a small circular region in the center of the SiO₂ layer was treated with 7% nitric acid in order to create a hydrophilic surface capable of accepting the aqueous nanoparticle solution. Ag nanoprisms capped with BSPP were drop-cast from solution and N₂ dried on the treated SiO₂. Another 1500 nm layer of SiO₂ was then deposited on the first SiO₂ layer containing nanoparticles. Placement of the nanoparticles near the lower region of the 1700 nm (total) layer of SiO₂ was necessary to assure visibility for imaging (SiO₂ transparency \leq ca. 1300 nm) and to decrease the likelihood of dielectric breakdown.

After the first SiO₂ deposition, the sample was exposed to acid and air for an extended period of time. Although SiO₂ should deposit cleanly on itself, exposure to the environment and the presence of nanoparticles likely created structural inconsistencies and impurities. To avoid dielectric breakdown caused by these impurities at the junction of the two deposition layers, the thickness of the top SiO₂ layer was maximized. Aluminum metal was then deposited on top of the second SiO₂ layer by thermal evaporation using a Denton Systems (Explorer series) vacuum chamber. All thin film depositions were performed in the clean room at the Center for Nano- and Molecular Science (CNM) at the University of Texas Austin. The top 200 nm layer of metal acted as the second plate in the capacitor, to which thin metal wire was attached with conductive epoxy. High voltage and ground leads from an Agilent 33220A function generator and an EMCO model Q101-5, 0.50 Watt, +10,000 DC volt maximum high voltage power supply were clamped to the sample wires to apply a potential. Silver nanoprisms were synthesized by Katherine Koen using a previously published protocol.²²

2.2 SAM INDUCED LSPR SHIFT OF GOLD NANORODS

2.2.1 Materials

Glass slides (25 x 25 x 1 mm) and a polydimethyl siloxane (PDMS) mixing kit were purchased from Sigma-Aldrich. Spectroscopy grade 200 proof ethanol was purchased from Fisher. The 11-amino-1-undecanthiol (MUAM) was purchased from Dojindo (Japan). Gold NRs were synthesized using sodium borohydride (NaBH_4), cetyltrimethylammonium bromide (CTAB), gold chloride (AuHCl_4), silver nitrate (AgNO_3), 99 % ascorbic acid and hydrochloric acid (HCl) (37 %) purchased from Sigma-Aldrich.

2.2.2 Sample preparation

All glass slides were rinsed with ethanol and plasma cleaned with argon for 30 minutes. An incubation chamber was carved from a PDMS mold. The PDMS frame and glass slide were O_2 plasma cleaned for 30 seconds, immediately attached and heated for several minutes at ca. 70°C for a secure seal. The chamber was designed to have an open top so that solution could easily be pipetted in and out. A solution of Au NRs in 0.1 M CTAB was pipetted into the incubation chamber and particles were allowed to stick to the glass surface for ca. 15 minutes. The aqueous solution was dried with N_2 and the Au NRs were washed with 700 mL of nanopure water to rid their surface of residual CTAB. In some cases Au NR samples were O_2 plasma treated for 30 seconds.

Gold NRs were synthesized using the following procedure. A seed solution and growth solution were prepared and mixed in varying ratios to obtain three Au NR solutions with slightly different plasmon locations. The seed solution was prepared by mixing 0.25 mL of HAuCl_4 with 9.75 mL of 0.1 M aqueous CTAB solution, adding 0.6 mL of ice cold 0.01 M NaBH_4 mixing rapidly for two minutes and allowing the solution

to sit for several hours. The growth solution was prepared by mixing 40 mL of 0.1 M CTAB solution and 2 mL of 0.01 M HAuCl_4 , adding 0.6 mL of 0.01 M AgNO_3 and 0.8 mL of 1 M HCl and finally adding 0.32 mL of 0.1 M ascorbic acid. Then a small amount of the seed solution was added to the growth solution. The larger the ratio of seed solution to growth solution the smaller the resulting particles.

2.3 DARK FIELD MICROSCOPY EXPERIMENTAL SET UP

Nanoparticle images were acquired using white light excitation from a halogen lamp source passed through a lens and directed to the sample with a 50/50 beam splitter at high angle in an off-axis, quasi-TIR geometry and in a through-the-objective design. An Olympus IX-71 microscope was used with an oil-immersion, high numerical aperture (NA = 1.45) objective. Any reflected excitation was rejected with a beam block, while low angle Rayleigh scattering was collected through the objective and imaged onto a Photonmax 512 electron multiplied charge-coupled device (EM-CCD). The image was magnified with a relay lens before reaching the CCD. In order to obtain an optimum signal-to-noise ratio, the TIR angle and beam stop position were adjusted for each sample and excitation source. The basic design used for nanoparticle imaging in the dark field is shown below in **Figure 1** in conjunction with the set up used for LSPR scattering spectra. To transition between dark field imaging and LSPR scattering spectra collection modes, a broadband polarizer (doubled Fresnel rhomb) and liquid crystal tunable filter (LCTF) were moved in and out of the white light excitation line.

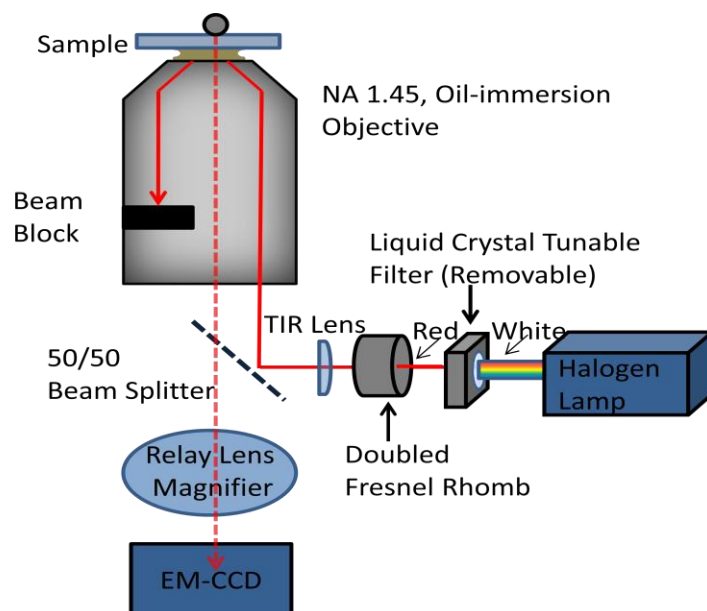


Figure 1. Experimental set up for imaging nanoparticles in the dark field and acquiring plasmon scattering spectra. Imaging particles was done using white light, while spectra were recorded by filtering white light with a doubled Fresnel rhomb and LCTF.

2.4 LSPR SPECTROSCOPY DATA COLLECTION

LSPR scattering spectra were obtained by filtering white light excitation with an LCTF to excite the nanoparticles one wavelength at a time. The scattering intensity was recorded for every wavelength over a 250 nm (450 nm – 700 nm) or 270 nm (450 nm – 720 nm) range, where each frame collected by the camera corresponds to plasmon excitation by one wavelength. A doubled Fresnel rhomb (broadband polarization rotator) was used with the LCTF to separately collect s and p polarizations, which were later added together to produce spectra of circular polarization at full intensity. Labview code developed by Dr. Katherine Willets and Dr. David Andrews was used to control the LCTF concurrently with Winspec software, which was used to image light collected by the CCD. A normalized lamp profile of the halogen excitation source was processed in Winspec for every sample. This profile data was then input into MATLAB code, called LCTF_widefield.m, for normalization of the LCTF spectra files. Each diffraction

limited spot imaged was processed with this code to subtract the local background for each spot separately. One diffraction limited spot was assumed to be a single particle until data processing suggested otherwise.

Spectra of the two orthogonal polarizations were combined in one of two ways. If stage drift caused a pattern mis-match in the region of interest between s and p polarizations, the s and p data was processed separately and backgrounds were subtracted individually in MATLAB and then added together afterward. If the pattern of the nanoparticles in one polarization could be overlaid to match the other, merge.m MATLAB code was used to merge the LCTF files before background processing. To calculate the plasmon wavelength maximum (LSPR λ_{\max}) fit_peak.m MATLAB code was used. The code operates by plotting the first derivative of each spectrum and assigning the zero crossing point as the maximum. The same MATLAB code used for peak fitting simultaneously calculated the error of the fit. About 90 % of the single particle peaks fit had an associated error value between 1 nm and 3 nm.

2.4.1 Single nanoparticle confirmation

When attempting to image single nanoparticles in the dark field, it is possible that what appears through the microscope eyepiece to be a single particle is actually a dimer (two particles aggregated together) or a cluster of particles. Because of the small nanoparticle size (average 100 nm) a diffraction limited spot originating from a single particle may be indistinguishable from light scattered by multiple emitters. The presence of a single particle was confirmed by a sharp, singly-peaked spectrum corresponding to the diffraction limited spot. Several measures were taken to ensure that particle deposition on glass slides resulted in single particles separated by much more than the diffraction limited spot size diameter. When aggregation became a problem, the

nanoparticle solution was sonicated for several minutes immediately before it was drop-cast onto glass.

Chapter 3: Dielectric Sensitivity of Silver Nanoprisms

3.1 INTRODUCTION

In this section the LSPR response of Ag nanoprisms to an external electric field is discussed. A brief overview of the purpose and procedure is given below in section 3.2 followed by the measurement technique and an experimental set up schematic in section 3.2.1. Results with discussion are provided in section 3.2.2, which compare observations for two different sets of data. The discussion details explanations for two separate observations with the proposal of possible mechanisms.

3.2 ELECTRIC POTENTIAL INDUCED SHIFT OF LSPR

This experiment was designed to monitor the LSPR response to a change in applied potential. A sample was prepared by embedding Ag nanoprisms in a layer of deposited SiO₂. The SiO₂ layer was between two highly conductive materials including a patterned indium tin oxide (ITO) glass slide on the bottom and a thin film of Al deposited on top. The SiO₂ insulation layer allowed the sample to behave as a parallel plate capacitor capable of holding and releasing charge. A large potential was applied across the sample, during which time LSPR spectra were taken in order to monitor the shift in maximum wavelength. The same microscope, objective and set up described previously were used and were connected to a function generator and high voltage power source to introduce a large DC voltage across the sample.

3.2.1 Measurement technique and experimental set up

Figure 2 shows the addition of the function generator and high voltage power supply to the basic experimental set up. In order to apply a several hundred volt

potential, an external high voltage source was used with a function generator to control the type (DC) and magnitude (voltage) of the bias.

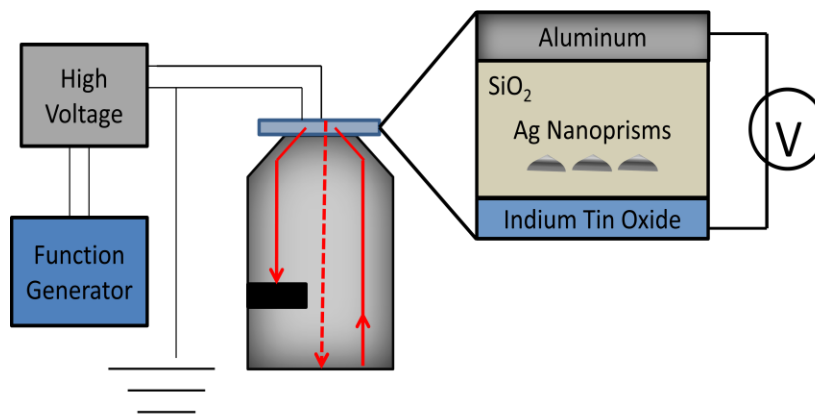


Figure 2. Sample geometry of potential application across the nanoparticle embedded thin SiO₂ layer. The red lines show single wavelength excitation (solid) and Rayleigh scattering (dotted).

While the sample was mounted on the microscope, a potential was applied with a function generator and high voltage power supply. LSPR data were taken using the LCTF and all of the same optics as described above. Filtration of white light from the halogen source with the LCTF is represented by red lines along the optical pathway. This shows a single excitation wavelength from the range of 450 nm – 700 nm with corresponding Rayleigh scattering.

The positive terminal of the voltage supply was connected to the aluminum electrode at the top of the sample and the negative ground was connected to the ITO electrode site. Each sample was tested prior to data acquisition to check for good lead connection and sufficient resistivity of the insulation layer. Spectra were recorded during 5 consecutive time intervals. Interval 1 corresponds to a time before the application of any potential (0 V) and intervals 2 through 5 respectively were (2) + 600 V potential, (3)

return to 0 V potential, (4) + 966 V potential and (5) return to 0 V. **Figure 3** below illustrates these intervals.

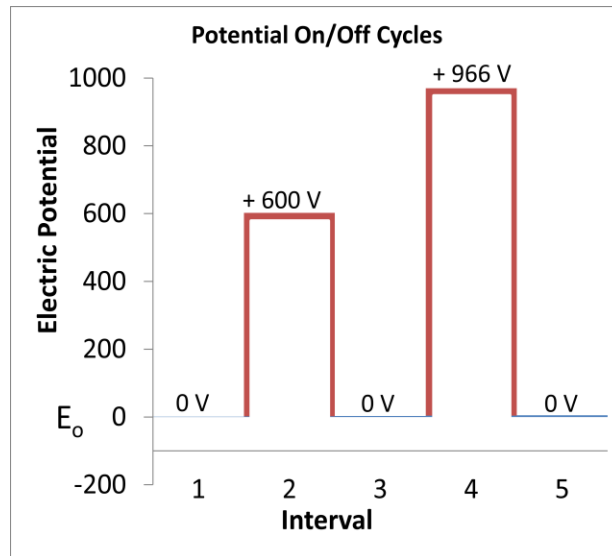


Figure 3. On/off cycles with the applied electric potential in volts over time. Three sets of spectra were taken during each of the five time intervals.

After each bias was applied to the sample the resistivity of the sample was probed to check for any dielectric breakdown that may have occurred during data acquisition.

3.2.2 Results and discussion

The sample used in this study was modeled as a parallel plate capacitor where the SiO_2 served as the insulation material between the ITO glass slide and Al deposition layer, which acted as two conducting plates. In principle, when a bias is applied across the plasmonic nanoparticles embedded in the SiO_2 , opposite charges should accumulate at either plate. Electrons in the nanoparticle should align in response to the charges and create a temporary dipole. This anisotropic behavior with increased local charge density should cause the LSPR wavelength maximum to shift reversibly as modulated with a bias.

Based on a calculation using Equation 3 above, the potential required to cause a measurable shift in LSPR was 600 volts and was predicted to be toward the blue.¹¹ At such large voltages it is unclear how a 1500 nm layer of deposited SiO₂ will be affected with respect to the dielectric breakdown. One result of dielectric breakdown is the formation of a conducting pathway between the two electrical connections. The SiO₂ crystallinity deposited by the Oxford deposition has a reported dielectric breakdown of > 5 MV/cm. Although we maintained a value of ≤ 5 MV/cm, the results suggested that the large potential may have influenced the SiO₂ structure. Based on the nature of the deposition techniques, the sample quality consistency was limited by instrumental performance. Both reversible and irreversible LSPR shifts were observed for two samples prepared using the same technique. This section provides discussion of both types of behaviors with explanation for possible causes.

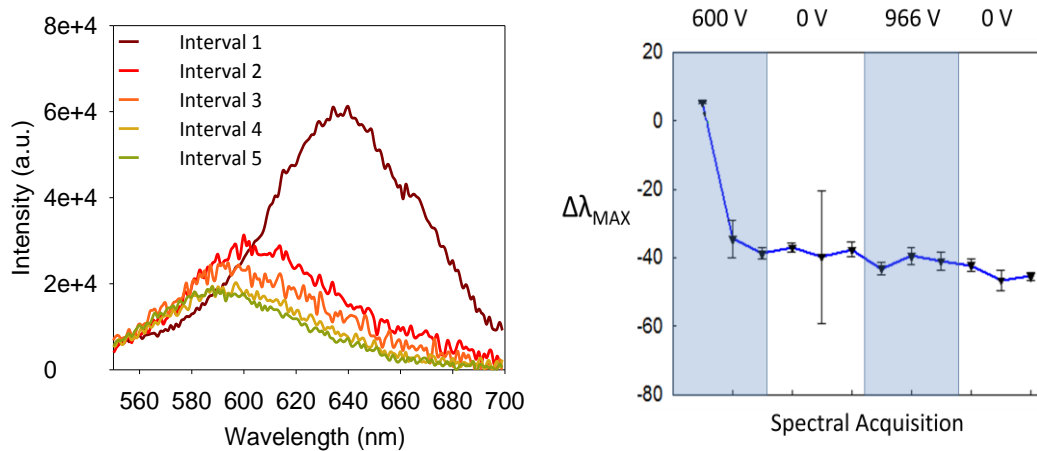


Figure 4. Plasmon resonance spectra of a single Ag prism embedded in deposited SiO₂ before, during and after exposure to a + 600 V and + 966 V potential are shown on the left. The LSPR shifting of the same single particle as the potential was adjusted is shown on the right over the course of one entire experiment.

We expected to see the LSPR reversibly shift as the electric field was switched on and off, however this was not observed for the sample represented in **Figure 4**. Here the

irreversibility of the LSPR shift of a single nanoprism is illustrated with spectra to the left and their corresponding LSPR $\Delta\lambda_{\text{MAX}}$ to the right plotted over the course of one experiment. The spectrum representing the plasmon before any applied voltage is of greater intensity and red-shifted ($\lambda \approx 640$ nm) compared to all successive spectra. The other four spectra correspond to intervals as defined by **Figure 3**. These on-off cycles were sequentially the following; +600 V (on), 0 V (off), +966 V (on) and 0 V (off). During each of these four intervals, spectra were recorded three times. The shift of each of the 12 spectra with respect to the initial pre-bias spectrum is plotted to the right in **Figure 4**. A negative shift in the LSPR λ_{MAX} corresponds to a blue shift. The experimental axis represents the span of time over the course of the experiment, but was not labeled specifically due to an inaccuracy of time. The purpose of recording multiple spectra within an interval was to track how the plasmon responded to the presence and absence of charges created by an electric field with respect to time.

The large irreversible shift at the onset of the first voltage application, followed by continual shifts in the same direction suggests that the structure of the SiO₂ surrounding this nanoparticle or the nanoparticle itself underwent permanent change. If the density or crystallinity of SiO₂ changed, there would be an associated change in dielectric causing an LSPR shift.²³ The large decrease in scattering intensity of the plasmon that occurred at the same time as the onset shift may indicate nanoparticle oxidation.²⁴ Oxidation induced by excessive heat can depend on the relative free energies of formation (ΔG_f) between the Si-O and Ag-O bonds.²⁵ Although oxidation was reported by Yanase et. al. to cause a red shift, there was an accompanying shape change, which was observed elsewhere to cause a blue shift.²⁶ The direction of LSPR shift is dependent upon how the shape changes and may have a dominant effect over that of an oxide layer.

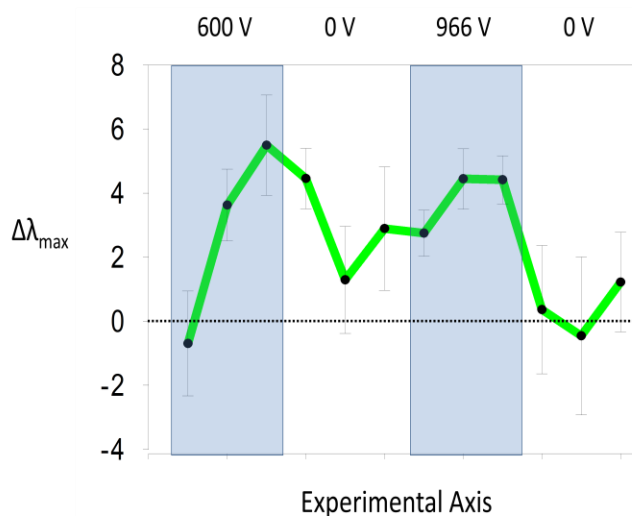


Figure 5. LSPR shifting behavior of a single Ag nanoprism over the course of the potential on-off cycles. Reversible behavior is illustrated.

Figure 5 displays reversible LSPR shifting, which we expected to observe. During the first +600 V bias period (left-most shaded region) it can be seen that the LSPR red shifted by about 6 nm. After the bias was turned off the LSPR blue shifted back toward its original position. When a larger +966 V bias was applied the LSPR again red shifted followed by a blue shift when that bias was turned off. Although reversible behavior was observed, other expectations were not met. Contrary to expectation, the observed shift was to the red. During the first off period, the LSPR λ_{MAX} did not blue shift all the way back to the original resonance position. For the second voltage on cycle, where the bias was 366 V larger than it was during the first, we expected a farther plasmon shift, however it shifted slightly less.

It is likely that the observed LSPR shifts were a combination of mechanisms including bias-induced anisotropy by surface charge rearrangement, degradation of the SiO₂, metallic surface oxidation and heating effects leading to particle shape change.^{25, 27}

Figure 6 below represents possible mechanisms responsible for the irreversible (shown

in **Figure 4**) and partially reversible (shown in **Figure 5**) behaviors of two single nanoparticles from different samples. The mechanism proposed for the data from **Figure 4** shows current passing through the SiO₂ layer as a result of dielectric breakdown. Here, no charge builds up on the sample plates because the insulation layer has been damaged. This could lead to irreversible LSPR shifting caused by either a decrease in the effective local dielectric or continued oxidation of the metallic surface. This was confirmed by the fact that the potential measured at the sample electrode was 0 V compared to the applied 600 V, indicating the flow of current.

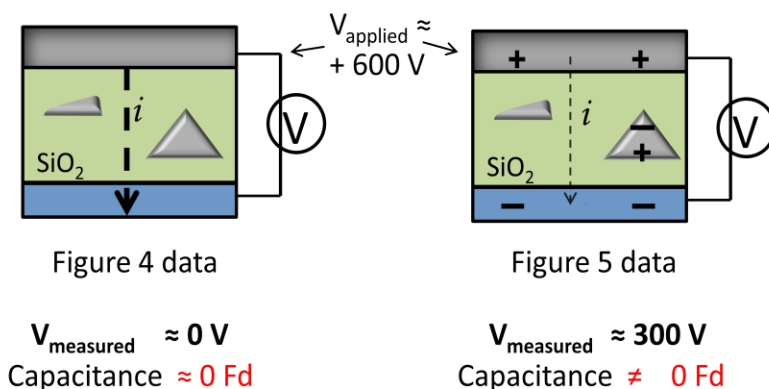


Figure 6. A pictorial representation of the possible mechanisms responsible for observed plasmonic Ag nanoprism response to an external potential when embedded in SiO₂.

In the mechanism proposed for the data from **Figure 5**, less current passes and particle surface electrons have an anisotropic response by aligning in opposition to charge accumulated on the sample plates. If the applied potential and measured sample potential are the same, this would indicate that the SiO₂ material is insulating, allowing no charge to pass. We observed a measured 300 V potential (half of the applied 600 V potential) at the sample electrode, which confirmed partial sample insulation (charge accumulation on the aluminum and ITO layers) with some current flow. Variation in particle orientation with respect to the sample plane could impact the way charge distribution changes the

LSPR for individual nanoprisms. This could explain how the competing mechanisms, charge anisotropy and dielectric breakdown, lead to partially reversible LSPR shifting.

3.3 CONCLUSION

In this experiment we investigated the sensitivity of plasmonic nanoparticles to a change in the external dielectric by measuring the LSPR λ_{MAX} shift due to an externally applied potential. Silver nanoprisms were imaged using dark field microscopy and LSPR spectra were constructed by tuning the wavelength of the excitation source. The Ag nanoprisms were embedded in SiO₂ and the LSPR spectra were taken while potentials of + 600 V and + 966 V were introduced. We observed both reversible and irreversible LSPR shifting behavior for single nanoparticles. We attribute these two behaviors to different responses of the SiO₂ layer to the high voltage bias. Irreversible LSPR spectral shifts were seen when dielectric breakdown of SiO₂ created a current passageway causing permanent structural change in the nanoparticle or surrounding material. Reversible LSPR spectral shifts were seen when the SiO₂ layer provided sufficient insulation such that charges accumulated on the conducting plates of the sample and the particle surface electrons responded. We have shown that nanoparticle surface plasmons can be modulated by introducing an electric field to their surrounding environment. This has important implications for the use of plasmonic nanoparticles in electronic and fuel cell devices.

Chapter 4: LSPR Sensitivity to a Self-Assembled Monolayer and Plasmon Enhanced Fluorescence

4.1 INTRODUCTION

The objective of this experiment was to monitor self-assembled monolayer (SAM) formation on Au NRs by imaging single molecule binding events. We aimed to image plasmon enhanced fluorescence using a dye-functionalized alkanethiol to form the SAM. The amine alkanethiol SAM molecule (MUAM) was modified with a fluorescent dye molecule (TAMRA). Previous to functionalizing the SAM molecule with a fluorescent dye, monolayer formation of the unmodified MUAM molecule was confirmed as part of a series of control experiments. This was achieved by observing shifts in the LSPR wavelength maxima due to dielectric sensitivity of Au NRs to a SAM. In addition, experimental conditions for the plasmon enhanced fluorescence study were optimized. These parameters were optimized as preliminary experiments in the series of controls.

Most SAM functionalized nanoparticle studies are performed by first forming the SAM on nanoparticles and then reacting the exposed end of the SAM molecule with another species of interest (e.g. fluorescent dye, quantum dots, proteins).²⁸⁻³⁰ Here, the SAM molecule was first reacted with a fluorescent dye, then allowed to diffuse through solution and adsorb to the nanoparticle surface. Structures of the SAM molecule (11-amino-1-undecanethiol (MUAM)) and fluorescent dye molecule (5-carboxytetramethylrhodamine succinimidyl ester (TAMRA)) used are shown in the experimental section in **Figure 7** below.

Materials and sample preparation relevant to the SAM induced LSPR shifts of Au NRs are outlined in section 2.2. Details of darkfield microscopy and LSPR spectroscopy are provided in sections 2.3 and 2.4 above. Section 4.2 below gives detail regarding materials, sample preparation, experimental set up and grazing angle reflection absorption infrared spectroscopy for the plasmon enhanced fluorescence study. Results and discussion for both the unmodified SAM induced LSPR shift and plasmon enhanced fluorescence studies are in sections 4.4 and 4.5 respectively.

4.2 EXPERIMENTAL

4.2.1 Materials

The 11-amino-1-undecanethiol (MUAM) purchased from Dojindo (Japan) and the 5-carboxytetramethylrhodamine succinimidyl ester (TAMRA) was purchased from Invitrogen. Dimethyl sulfoxide (DMSO) was purchased from Sigma-Aldrich. All other sample materials as described for the unmodified SAM study were used here.

4.2.2 Synthesis of dye functionalized SAM molecule

All sample preparation techniques were identical to those in the unmodified SAM study in 2.2.2 with exception of the synthesis of the fluorescent dye functionalized SAM described below. The succinimidyl ester group of the amine-reactive dye, TAMRA, reacts readily with the primary amine of the MUAM molecule to create a stable amide bond. N-hydroxysuccinimide (NHS) ester functionalized molecules can be used reliably to synthesize compounds with an amide bond because they have a high reactivity and specificity. Molecules containing the NHS ester derivative react with nucleophiles to form an acylated group and NHS leaving group. This reaction yields very stable conjugates that do not hydrolyze in an aqueous environment. The NHS ester group on the TAMRA dye makes it insoluble in aqueous solvents so DMSO was used. MUAM

was soluble in pure ethanol after sonication. Concentrations of ca. 1 mM of TAMRA in DMSO and ca. 1 mM MUAM in ethanol were reacted in ratio ranging from 1:1 – 3:1 MUAM:TAMRA at room temperature overnight. This reaction is promoted by pH levels in the range of 8.0 – 8.5, however due to the TAMRA water insolubility an aqueous buffer could not be used. The effective pH of the non-aqueous 1:1 mixture of ethanol to DMSO was 8.3, suitable for the reaction. Structures of the molecules and their reaction are depicted below in **Figure 7**.

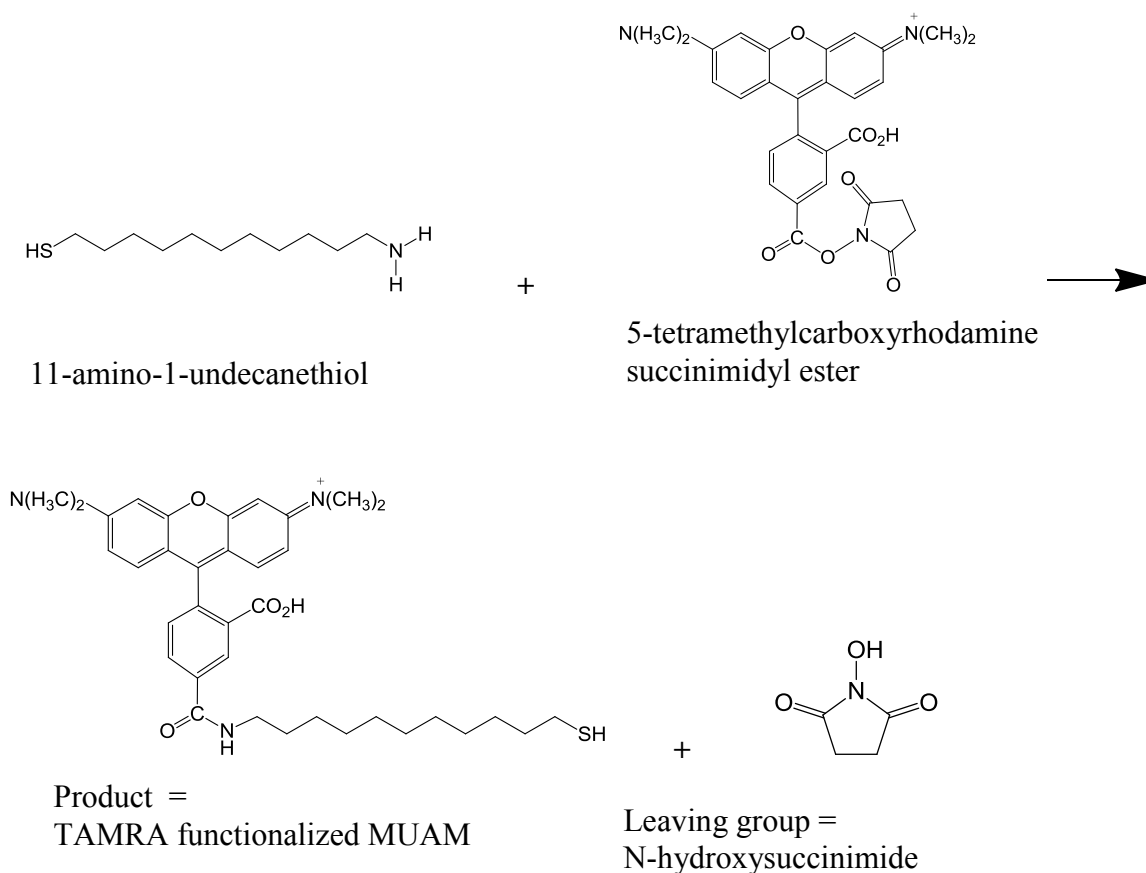


Figure 7. Reaction between the fluorescent dye 5-carboxytetramethylrhodamine succinimidyl (TAMRA) and the amine-modified SAM molecule 11-amino-1-undecanethiol (MUAM) to form a stable amide bond.

Amide formation by nucleophilic attack of the primary amine of 11-amino-1-undecanethiol on the succinimidyl ester group of 5-carboxytetramethylrhodamine succinimidyl ester proceeds as shown above. The reacted product was an 11 carbon alkanethiol chain with a secondary amine conjugated to the dye molecule carbonyl in place of the succinimidyl ester oxygen of the unmodified dye. Upon reaction the rhodamine derivative retains its heterocyclic fluorone core structure common to the rhodamine dye family. N-hydroxysuccinimide (NHS) is the leaving group in the reaction.

4.2.3 Fluorescence experimental set up

In **Figure 8** below a schematic shows the introduction of a 20 mW 532 nm CrystaLaser (GCL-020-532-S) cw laser to the sample through a coupled fiber and 532 nm quarter wave plate. The excitation signal was sent to the microscope with a dichroic beam splitter, which replaced the flip mirror used for white light excitation, through the same TIR lens described previously.

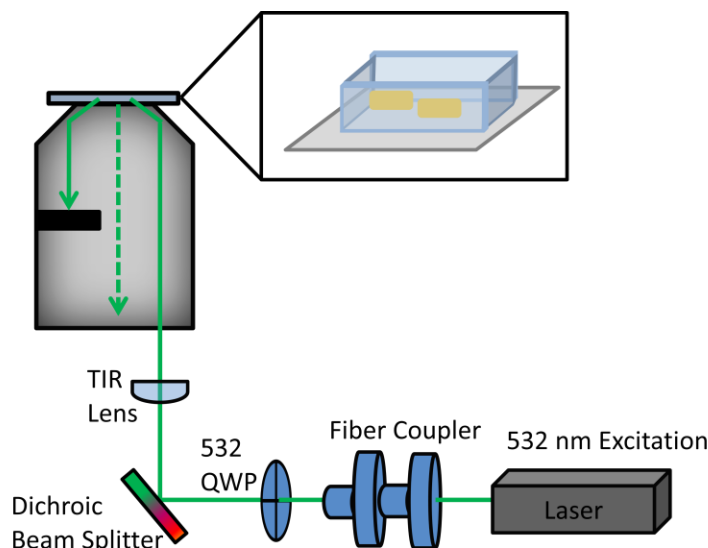


Figure 8. Laser excitation schematic with a PDMS incubation chamber mounted on a Au NR sample.

The 20 mW laser was coupled into a fiber and the measured output power at the microscope entrance was ca. 800 μ W. With the laser illumination in TIR the light should exponentially decay from the glass surface to several hundred nanometers above the sample plane, well encompassing the nanoparticles and all dynamics of interest. An enlargement of the Au NR sample with the incubation chamber is shown.

4.2.4 Grazing angle reflection absorption infrared spectroscopy

Attachment of MUAM to TAMRA by amide bond was confirmed by solid sample grazing incidence angle reflection-absorption infrared (GRAS IR) spectroscopy of the reactants and product. Analyte solution was drop-cast onto a surface deposition layer of gold and allowed to evaporate. IR spectra of pure MUAM, pure TAMRA and a reaction of MUAM and TAMRA were recorded and analyzed. The IR data was collected using GRAS-IR in the Webb research lab at the University of Texas. Surface vibrational spectra were taken with a Bruker Vertex 70 GRAS IR spectrometer equipped with a A518/Q Horizontal Reflection (Bruker) for sample illumination at a grazing angle of 80

degrees. The sample chamber was purged with N₂ for one hour before and during data collection to reduce interference from H₂O and CO₂. Two rounds of data collection were taken on different detectors each using 100 scans. The mercury cadmium telluride (MCT) detector scanned from 400 cm⁻¹ to 4000 cm⁻¹ optimal for the amide carbonyl peak region from ca. 1550 cm⁻¹ to 1700 cm⁻¹. The second, indium antimonide (InSb), detector scanned from 1870 cm⁻¹ to 4000 cm⁻¹ optimal for the N-H peak region from ca. 3000 cm⁻¹ to 3500 cm⁻¹. Spectra were analyzed by background subtraction of pure Au surface scans, baseline flattening with a polynomial function and peak integration with OPUS software.

4.3 DARK FIELD IMAGES AND LSPR SPECTRA

Representative Rayleigh scattering images of single Au NRs acquired using dark field microscopy are shown on the left of **Figure 9** below with representative LSPR spectra on the right. These spectra correspond to Au NRs from the same sample and are indicated in the white light image with circles. Their average LSPR $\lambda_{\max} \approx 635$ nm and these particles have an estimated aspect ratio of ca. 2.9, which is discussed in detail in section 4.4.2.1.

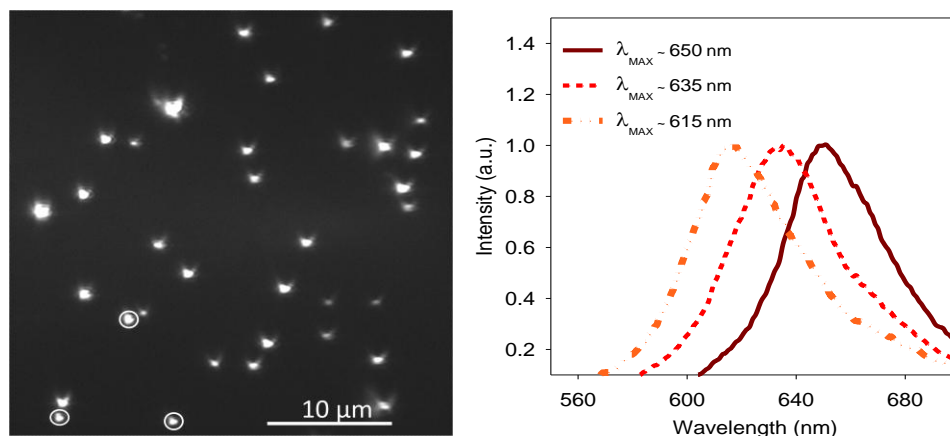


Figure 9. White light Rayleigh scattering of Au NRs imaged under N₂ is shown on the left and single particle scattering spectra corresponding to the three circled diffraction limited spots are shown on the right.

Nanorods have two plasmon resonance modes; the longitudinal mode which oscillates along the long axis of the rod and the transverse mode which oscillates along the short axis of the rod. Often, only the longitudinal mode is measured because the signal from the transverse plasmon mode is too weak to observe, as for our case. The longitudinal plasmon was sensitive to excitation polarization and all fitted peak maxima were the addition of s and p polarized excitation light, as shown in spectra in **Figure 9** to the right. Sources of uncertainty in the LSPR wavelength maximum ($\Delta\lambda_{MAX}$) are related to signal-to-noise, polarization and peak broadening.

4.4 SAM INDUCED LSPR SHIFT

This experiment was designed to detect the shift of Au NR plasmons induced by formation of a SAM on the particle surface. The purpose of this study was two-fold; first to detect the monolayer formation on the Au surface during nanoparticle incubation in SAM solution and second to optimize the conditions of a developing experiment which will image plasmon enhanced fluorescence from dye-functionalized SAM molecules during monolayer formation. The detection of an unmodified SAM layer by LSPR spectral shifting was a control for the modified SAM study. The same microscope,

objective and set up described previously were used for both studies and a cw 532 nm laser was introduced to the same optical path for the fluorescence study.

4.4.1 Measurement techniques

Controls were performed in order to both investigate the independent effects of experimental parameters and to verify formation of the SAM. The parameters considered were solvent effect and O₂ plasma treatment of the Au NRs. Three different control techniques were used to investigate the solvent effect on nanoparticles. The first control was performed by the following steps: (1) ethanol incubation for 1 hour, (2) solvent removal and N₂ drying for 30 minutes, (3) LSPR spectra measurement in a N₂ environment and (4) repeat steps 1-3. The second control was performed by the following steps: (1) ethanol incubation, (2) LSPR spectra measurement right after ethanol addition, (3) LSPR spectra measurements every 15 minutes until the λ_{MAX} stops shifting. The third control was the O₂ plasma treatment of Au NRs intended to remove any residual CTAB or other surface contaminant. Oxygen plasma treatment was done moments before data acquisition.

For the SAM formation controls, the 11-amino-1-undecanethiol (abbreviated MUAM) solution was used under the same conditions as the second control experiment. The SAM formation was performed by the following steps: (1) ethanol incubation for one hour, (2) LSPR spectra measurement in ethanol, (3) SAM solution incubation for 1 hour, (4) removal of SAM solution and 5 pure ethanol washes, (5) pure ethanol incubation, (6) LSPR spectra measurement in ethanol.

4.4.2 Discussion

4.4.2.1 Gold nanorod characterization

Three different sizes of Au NRs were synthesized using a combination of procedures based on those developed by Chen et al. and Mayer et al.^{31, 32} The specifications of the procedure are outlined above in Chapter 2. The variation in NR size and aspect ratio (AR) was a result of the ratio of seed to growth solution in the synthesis process. To estimate the aspect ratio of the Au NRs, the longitudinal mode wavelength maxima were compared with literature values reported by Huang et al.³³ The peak near 750 nm is indicative of NRs with an aspect ratio of about 3.5, the peak near 700 nm is indicative of NRs with an aspect ratio of about 2.9 and the peak near 670 nm an aspect ratio of about 2.5.

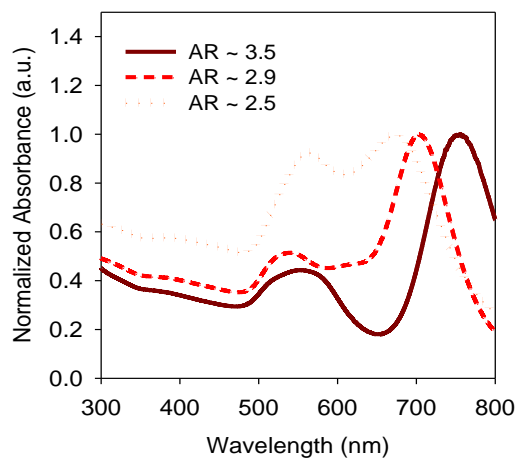


Figure 10. UV-Vis spectra of Au NRs in 0.1 M CTAB solution. The LSPR of the transverse and longitudinal modes respectively for three different particle growth samples with AR 3.5, 2.9 and 2.5 are $\lambda \approx 550$ nm & 750 nm, $\lambda \approx 540$ nm & 700 nm and $\lambda \approx 560$ nm & 670 nm.

The plasmon resonances of these particles in ethanol taken by darkfield spectroscopy (section 4.3 above) are blue-shifted compared to the UV-Vis spectrum shown in **Figure 10** because of the high concentration of CTAB present in the liquid sample.³⁴ Spectra of all three bulk Au NR samples show two peaks. The larger peak

near 700 nm represents the longitudinal mode, which is caused by plasmon oscillation along the long axis of the nanorod. The smaller peak near 550 nm represents both the transverse mode oscillation along the short axis of the nanorod and the presence of a small sphere population. The transverse plasmon peak is known to absorb near 520 nm and be independent of nanorod aspect ratio. The wavelength maximum of the smaller peak in this case absorbs about 30 nm to the red of the characteristic transverse mode because of residual spheres in the solution. Variation in sphere size is responsible for the peak broadening. Consistent with expectations, the transverse mode varies much less with aspect ratio than the longitudinal mode. In **Figure 10** samples with AR of ca. 3.5 and 2.9 show twice the absorption of the longitudinal peak compared to that of the transverse peak in contrast to the sample of AR ca. 2.5 where the difference between the two peaks is only about 7%. That is likely due to a much smaller population size difference and particle size and aspect ratio difference between the two types of nanoparticle populations (spheres and rods) for the sample with estimated AR ca. 2.5. The sharpness of the 560 nm peak in the AR ca. 2.5 sample probably indicates a lower relative size variation for that particle population.

4.4.2.2 Control experiments and SAM modified LSPR shift

We performed control experiments that tested for solvent effect and the effect of O₂ plasma treatment on the Au NRs. We expected to see a blue shift in the LSPR over time during solvent incubation, based on previous results.²⁶ An LSPR shift caused by solvent exposure could originate from two effects. Solvent molecules adsorbed to the particle surface could lead to spectral shifts through either a change in the external dielectric (red shift) or a change in particle shape driven by the relative surface tensions (free energy per unit area) at the interfaces of particle surface/substrate, substrate/solvent

and particle surface/solvent.²⁶ After these controls SAM experiments were performed. We expected to see a red shift in the LSPR.²⁶ The experimental steps for samples 1-8 in the table in **Figure 11** are summarized.

The measurement steps for samples 1 and 2 were: (1) LSPR spectra taken under N₂, (2) ethanol incubation for one hour, (3) N₂ drying for 30 minutes, (4) LSPR spectra under N₂ and (5) repeat steps 2-5.

The measurement steps for sample 3 were: (1) O₂ plasma treatment for 30 seconds, (2) LSPR spectra taken under N₂, (3) ethanol incubation for one hour, (4) N₂ drying for 30 minutes, (5) LSPR spectra under N₂ and (6) repeat steps 2-5.

The measurement steps for samples 4 and 5 were: (1) O₂ plasma treatment for 30 seconds, (2) LSPR spectra under N₂, (3) ethanol incubation for one hour, (4) N₂ drying for 30 minutes, (5) LSPR spectra under N₂, (6) SAM solution incubation for one hour, (7) 5 pure ethanol wash cycles, (8) N₂ drying for 30 minutes and (9) LSPR spectra under N₂.

The measurement steps for sample 6 were: (1) LSPR spectra under N₂, (2) ethanol incubation for five minutes, (3) LSPR spectra during ethanol incubation, (4) ethanol incubation for one hour and (5) LSPR spectra during ethanol incubation.

The measurement steps for samples 7 and 8 were: (1) LSPR spectra under N₂, (2) ethanol incubation (3) LSPR spectra taken during ethanol incubation starting five minutes later until spectral shifting stopped, (4) SAM incubation for one hour, (5) 5 pure ethanol wash cycles, then pure ethanol incubation and (6) LSPR spectra during ethanol incubation.

Counter to expectation, no measureable LSPR shift was observed after one hour of incubation in solvent (ethanol). However, we did observe a red shift in the LSPR due to SAM formation as expected. Other observations made regarding the control experiments are as follows. The LSPR of Au NRs treated with O₂ plasma for 30 seconds

were compared with LSPR spectra of untreated NRs (data not shown). There was no significant difference in the distribution of λ_{MAX} for the treated versus un-treated samples taken under N_2 . However, differences in $\Delta\lambda_{\text{MAX}}$ were observed for untreated versus O_2 plasma treated samples after solvent incubation. This is shown in **Figure 11** by comparison of the average shifts of all nanoparticles in samples 2 and 3 in the table below. The LSPR of particles that were not O_2 plasma treated shifted to the red by ca. 4 nm after solvent incubation, while particles that were O_2 plasma treated for 30 seconds shifted to the red by ca. 20 nm after solvent incubation. It is possible that the removal of CTAB from the metal surface provided a platform capable of supporting more solvent molecules, which resulted in a greater effective dielectric. An interesting result arises from the comparison of samples 3 and 4, which were both O_2 plasma treated and exposed to solvent. Sample 3 was exposed to solvent *without* SAM molecules and a 20 nm *red* shift was observed. In contrast, sample 4 was exposed to solvent *with* SAM molecules and a 25 nm *blue* shift was observed. For samples 6, 7 and 8, where there was no drying cycle, spectra were taken while submerged in pure ethanolic solution and an LSPR red shift that increased with SAM concentration was observed. For samples 7 and 8, the SAM solution was washed thoroughly and samples re-suspended in ethanol in order to rid the Au surfaces of any unbound SAM molecules.

Sample	O ₂ plasma treated (seconds)	dry cycle	SAM [conc]	LSPR $\Delta\lambda_{\text{MAX}}$ (-)blue	LSPR $\Delta\lambda_{\text{MAX}}$ std dev
1	0	Y	none	9	6
2	0	Y	none	4	2
3	30	Y	none	20	4
4	30	Y	0.1 μM	-25	3
5	30	Y	1 μM	-35	5
6	0	N	none	0	1
7	0	N	23 μM	1	2
8	0	N	1250 μM	4	2

Figure 11. Comparison of the different average LSPR shifts under varying experimental conditions.

It is known that a monolayer will change the effective external dielectric to which the plasmonic nanoparticles are exposed, changing the position of the LSPR.²⁶ The amount by which the dielectric changes, and therefore the LSPR shifts, is dependent upon the chain length of the SAM molecule. The shifts caused by SAMs of chain length up to ca. 2 nm on the surface of Ag nanoparticles were estimated by Malinsky et. al. using a linear regression fit. They used seven different alkane thiols chain lengths between 3 and 15 carbons and observed $\Delta\lambda_{\text{max}}$ toward the red ranging from 2 nm to 40 nm. The authors observed a linear red shift in the LSPR with increasing alkane chain length described by the equation $y = 3.3x - 9.3$ where y is $\Delta\lambda_{\text{LSPR}}$ and x is the number of ethylenes in $\text{CH}_3\text{CH}_x\text{SH}$. Based on the 11-carbon atom SAM we predicted a shift of about 24 nm for full coverage. The reason we observe a much smaller red shift is probably because of incomplete surface coverage of the monolayer. In comparing samples 7 and 8, we observed a larger LSPR shift for a higher SAM concentration, likely caused by the partial monolayer coverage. The average LSPR shifts for samples 6 (no SAM) and 8 (1.25 mM SAM) in the table are 0 nm and 4 nm respectively. Histograms in **Figure 12** show the distributions of shifts for all the nanoparticles analyzed in samples 6 and 8. This

distribution is attributed to differences in monolayer formation due to particle variation originating from the growth process.

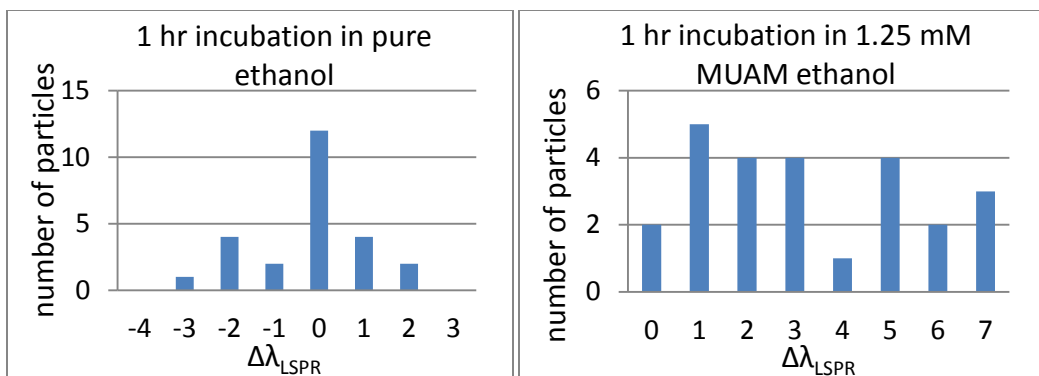


Figure 12. Histograms quantifying AuNRs LSPR shift of particles incubated in pure ethanolic (left) and 1.25 mM SAM (11-amino-1-undecanethiol) (right) solutions.

The LSPR of Au NRs exposed to different external dielectric environments is shown in **Figure 13** with spectra representative of ensemble averages. The three spectra (N_2 , ethanol and SAM) exhibit nanoparticle plasmon resonance from Au NRs under N_2 , after incubation in pure ethanolic solution and after SAM formation of MUAM with re-suspension in pure ethanol. The measurement steps for these particles were identical to those for samples 7 and 8, where spectra were taken in N_2 , the sample was incubated in pure ethanol for one hour while spectra were taken periodically, a SAM of MUAM was formed for one hour, the sample was washed 5 times with pure ethanol followed by re-suspension in pure ethanol and finally LSPR spectra were taken.

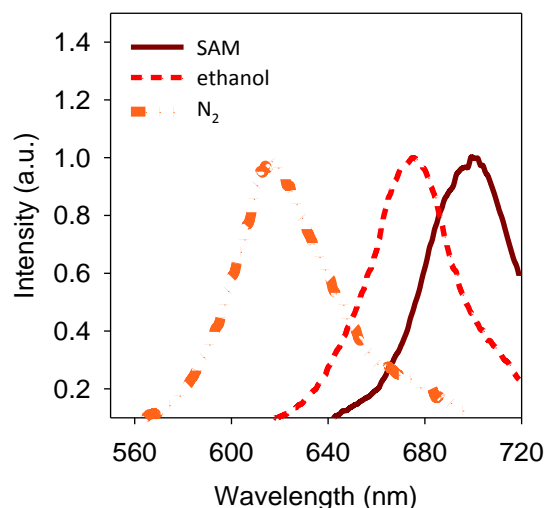


Figure 13. Representative LSPR spectra of the longitudinal plasmon mode for Au NRs in N₂, ethanol and modified with a SAM (11-amino-1-undecanethiol).

The average spectral shift of the LSPR of an ensemble of Au NRs from N₂ to ethanol was ca. 45 nm to the red and the shift from unmodified to SAM modified Au NRs in ethanol was ca. 4 nm to the red. A farther red shift, beyond that caused by ethanol, due to the SAM is expected because the SAM layer is in contact with the nanorod surface in the region where a change in the external dielectric has the most impact on the position of the plasmon. If the SAM had completely covered the nanoparticle surface an LSPR shift of more than 4 nm would likely have been observed.

4.5 DYE FUNCTIONALIZED SAM FLUORESCENCE

4.5.1 Grazing Angle Reflection Absorption Infrared Spectroscopy analysis

Solid GRAS IR was used to confirm the reaction between 11-amino-1-undecanethiol (MUAM) and 5-carboxytetramethylrhodamine succinimidyl ester (TAMRA). GRAS IR spectra of the reactants, MUAM and TAMRA molecules, were compared to that of the product shown below in **Figure 14**. Equivalent concentrations of pure dye solution $[C]_{\text{dye}}$ and dye in the dye-functionalized SAM solution $[C]_{\text{dye-SAM}}$ were

verified by UV-Vis absorption and used for IR analysis. Enlarged IR peak regions are provided where necessary throughout analysis.

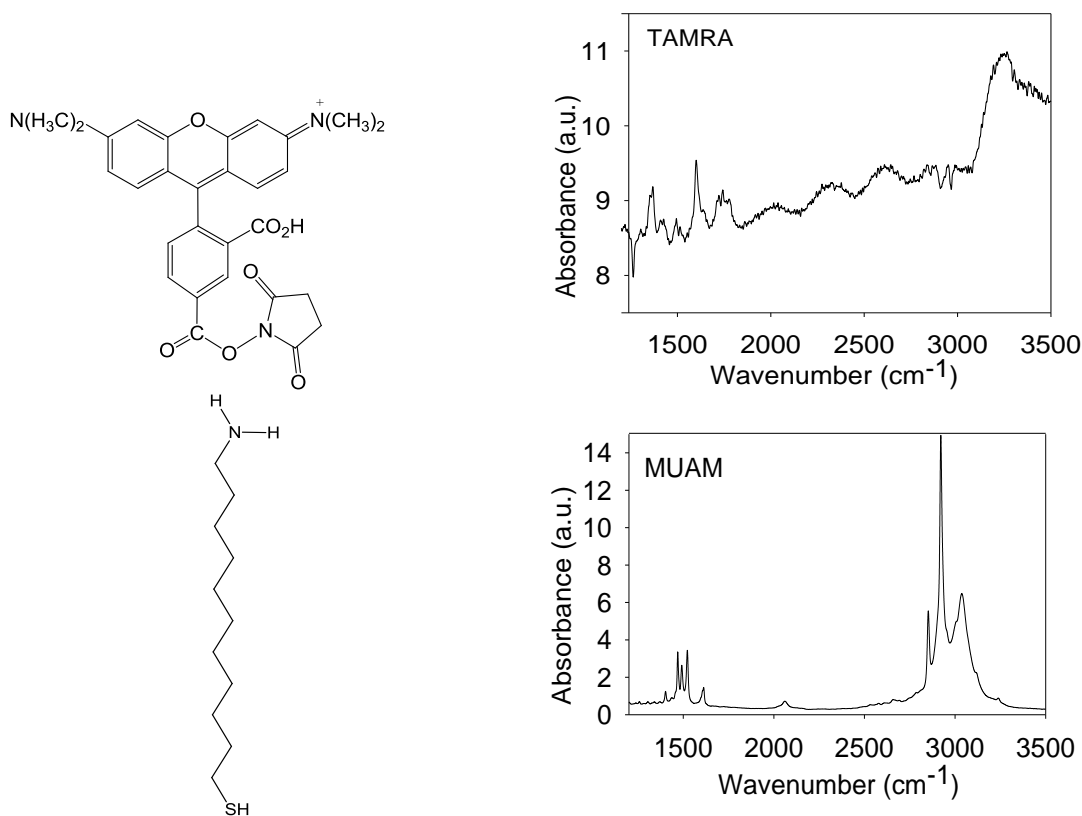


Figure 14. Solid GRAS IR of the amine reactive dye (5-carboxytetramethylrhodamine succinimidyl ester)(top) and SAM molecule (11-amino-1-undecanethiol) (bottom).

For clarity **Figure 15** shows a magnification of the IR spectra from 1400 cm⁻¹ to 1800 cm⁻¹ of the pure TAMRA dye, MUAM SAM molecule and TAMRA-MUAM product. Evidence that the reaction proceeded is given by two peaks labeled in the TAMRA-MUAM IR spectrum near 1550 cm⁻¹ and 1650 cm⁻¹, characteristic of an amide bond for similar structures where peaks at 1550 cm⁻¹ and 1660 cm⁻¹ are assigned as the two amide bond peaks.^{35, 36} These peaks are weaker than others in the reactant molecule spectrum, but that is expected due to incomplete reaction leading to lower relative abundance. The TAMRA-MUAM spectrum also has a weak peak at 1636 cm⁻¹, which

could be coming from the amide bond or an amide bond split based on its proximity to the 1650 cm^{-1} peak. The adjacent 1615 cm^{-1} peak in the TAMRA-MUAM spectrum is from the 1615 cm^{-1} peak in the pure MUAM spectrum. In addition to the appearance of amide bond frequencies, the disappearance or reduction of NH_3^+ frequencies provides evidence for successful reaction. Quantification of peaks results in large uncertainty due to the inconsistency of sample drying in the solid IR preparation technique and is therefore not analyzed. What can be considered is the change in the relative strength of two peaks that both appear in two different spectra. Frutos et. al. observed peaks in their MUAM spectrum near 1610 cm^{-1} and 1514 cm^{-1} which they assigned to the asymmetric and symmetric NH_3^+ stretches respectively. We observed peaks in our MUAM spectrum close to both of these near 1615 cm^{-1} and 1522 cm^{-1} and assigned these to NH_3^+ stretches. The fact that the relative intensities of these two peaks in the MUAM spectrum ($1522\text{ cm}^{-1} > 1615\text{ cm}^{-1}$) changed in the TAMRA-MUAM spectrum ($1615\text{ cm}^{-1} > 1522\text{ cm}^{-1}$) is indicative of the reduction in an NH_3^+ vibration and corresponding amine group reaction. In another MUAM spectrum, Wallwork et. al. observed a peak near 1607 cm^{-1} assigned to both N-H bending and C-N stretching.³⁷ Some C-N stretching could contribute to the strength of our 1615 cm^{-1} peak in the TAMRA-MUAM spectrum. The carbonyls on the NHS group should absorb above 1700 cm^{-1} and not interfere.³⁸ Due to incomplete reaction, the carbonyls on pure TAMRA molecules likely contributed to peaks in the region of interest. There is a peak in the TAMRA-MUAM spectrum at 1710 cm^{-1} possibly due to the amide carbonyl as seen in literature.³⁹ The authors also observe an amide CHN vibration near 1544 cm^{-1} compared to a 1550 cm^{-1} peak in the TAMRA-MUAM spectrum, which we assign as an amide.

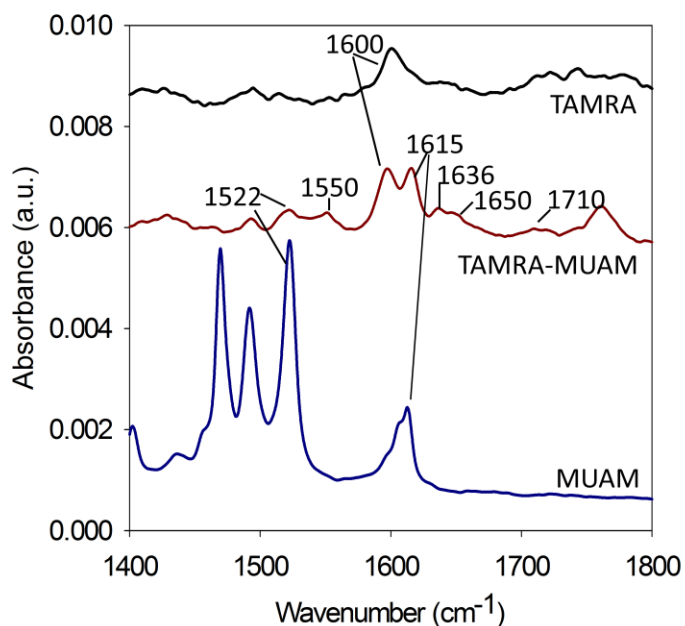


Figure 15. Magnification of the peak region $1400\text{ cm}^{-1} - 1800\text{ cm}^{-1}$ of GRAS IR spectra of the amide-containing product of SAM (11-amino-1-undecanethiol (MUAM)) and dye (5-carboxytetramethylrhodamine succinimidyl ester (TAMRA)), the pure TAMRA and pure MUAM.

Figure 16 provides further proof of bond formation through negative evidence as the strong N-H bond stretch peak near 3040 cm^{-1} appearing in the spectrum of pure MUAM is absent in the TAMRA-MUAM spectrum. This indicates that many of the N-H groups are absent due to reaction with the carbonyl of TAMRA. The strong 3250 cm^{-1} peak could be in part from a carboxylic acid group on the dye molecule as a strong peak appeared there in the spectrum of the pure dye (TAMRA). However, we suspect that much of this peak is coming from the N-H stretch from an amide bond. Secondary amides have only one N-H bond stretch that was most often observed near 3250 cm^{-1} upon inspection of IR spectra for numerous other amides.⁴⁰ This is consistent with the TAMRA-MUAM spectrum expected to contain an amide bond and which has a strong peak near 3248 cm^{-1} . Primary amines have two IR bands, one for the symmetric stretch near 3300 cm^{-1} and another for the asymmetric stretch near 3400 cm^{-1} . Our sample of

MUAM contains a stabilizing HCl population. Amine complexation with hydrogen halides is known to cause vibrational shift.⁴¹ By inspection of numerous other primary amine IR spectra with and without the presence of HCl, it seems that N-H absorption with HCl shifts both symmetric and asymmetric stretches to lower wavenumbers near 3100 cm^{-1} and 3300 cm^{-1} respectively.⁴⁰ This could explain why the strong peak in the MUAM spectrum assigned to N-H stretches is closer to 3100 cm^{-1} than the characteristic 3400 cm^{-1} . Another reported spectrum of pure MUAM shows only one peak above 3000 cm^{-1} at 3416 cm^{-1} , which is in support of the 3040 cm^{-1} peak assignment to N-H stretches shifted by the presence of HCl.³⁷ One disadvantage of the solid IR technique is the interference pattern created by instrumentation, which appears clearly in the TAMRA-MUAM spectrum in **Figure 16** between ca. 1900 cm^{-1} and 2750 cm^{-1} . The interference pattern is created by constructive and destructive interference between the reflected and refracted signals, which is dependent on sample thickness, refractive index, angle of incidence and polarization. This created difficulty in peak recovery.

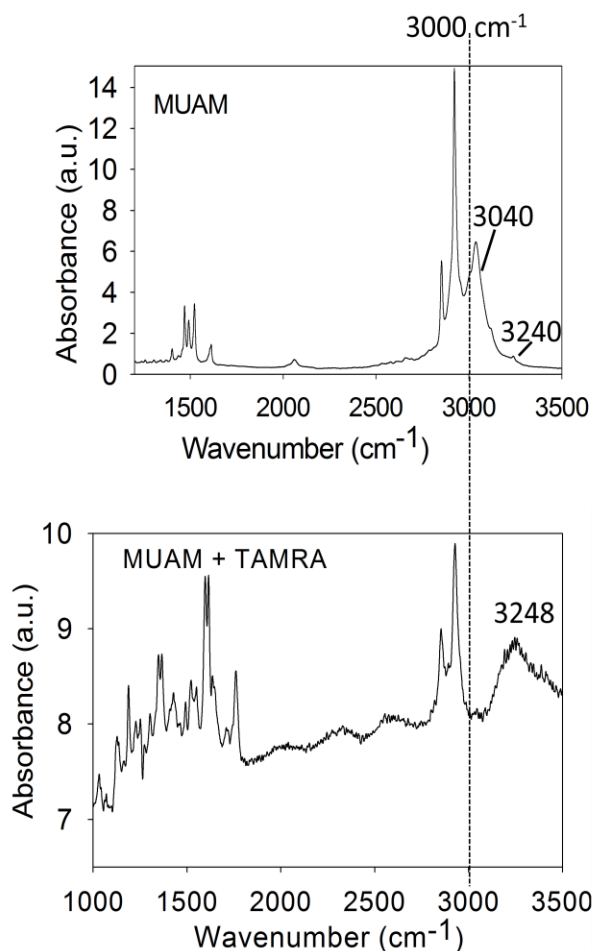


Figure 16. GRAS IR spectra of pure SAM (MUAM) (top) and dye-functionalized SAM (TAMRA-MUAM) (bottom) display the disappearance of the 3040 cm^{-1} N-H peak upon reaction. A dotted line at 3000 cm^{-1} was added to help guide the eye.

4.5.2 TAMRA-MUAM diffusion and SAM formation on Au NRs

Dye-functionalized SAM formation on the Au NR surface was carried out with identical parameters to the experiment outlined above, except the pure SAM was replaced with the dye-functionalized SAM. The 532 nm cw laser was used to excite a TAMRA-MUAM solution as the functionalized SAM molecules diffused through solvent within the sample incubation chamber and their thiol groups bound to the Au NR surface. When the TAMRA-MUAM molecule diffused close to the nanoparticle surface it was exposed

to both the surface plasmon and an exponentially increasing evanescent laser wave. In this vicinity, the dye molecule released a bright burst of plasmon enhanced fluorescence. Upon contact with or adsorption to the nanoparticle surface the molecule became quenched.⁴² The experimental process is pictured below in **Figure 17**.

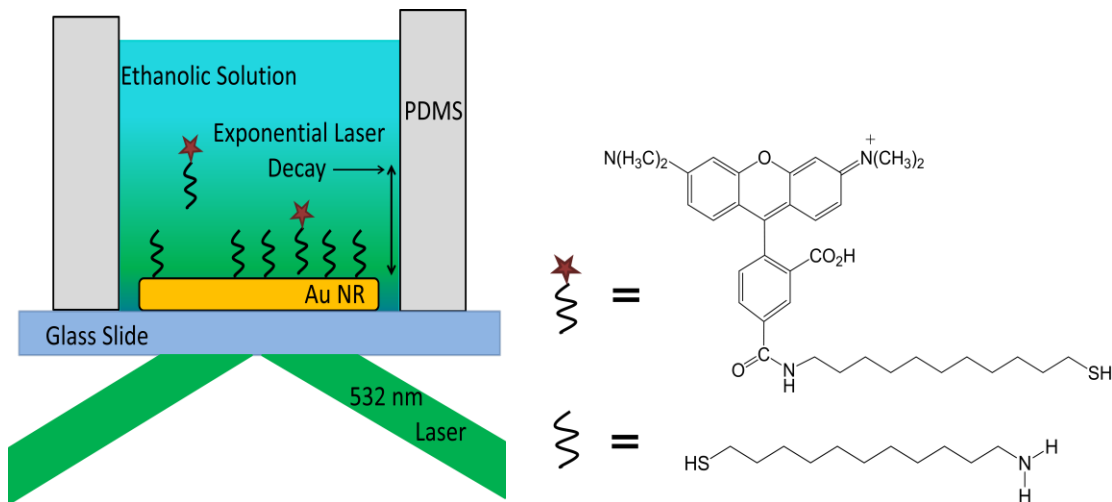


Figure 17. Representation of the dye-functionalized SAM forming on the Au NR surface as it diffuses through solution within an incubation chamber under TIR laser illumination.

4.5.3 TAMRA-MUAM fluorescence

Au NRs on glass were incubated in an ethanolic solution of the dye-functionalized SAM to allow diffusion through solution and subsequent monolayer formation. During the incubation period a 532 nm laser was used to excite fluorescence in the dye-functionalized SAM as it approached the Au NR surface; a region of increased laser evanescence intensity and plasmonic enhancement. Plasmon enhanced fluorescence events were recorded with the CCD camera using 100 ms – 300 ms acquisition for about 3 minutes at a time. This was the fastest acquisition rate that gave a large enough signal-to-noise ratio to observe dynamics.

Several concentrations and ratios of the pure MUAM and TAMRA solutions and acquisition rate were combined in order to optimize conditions for data collection. If the concentration of dye molecules in solution was too large the fluorescence from molecules in close nanoparticle proximity overwhelmed the detection signal. If the dye concentration was too low interesting dynamics did not occur frequently enough for timely data collection. Concentrations between 10 nM and 1.5 μ M were tested. The most useful optical dynamics were obtained for a concentration of 100 nM. The MUAM:TAMRA ratio was varied and it was determined that the most favorable range was between 1:1 and 3:1. The camera acquisition rate was varied from 50 ms to 500 ms and the most favorable trade off between good signal-to-noise and fast collection rate was observed from 100 ms to 300 ms. Because it was established that solvents cause LSPR shifting effects only when the drying step was included a solvent ratio in range of 1:1 to 3:1 ethanol:DMSO can be used for SAM formation. The presence of DMSO caused the effective pH of ethanol to increase from ca. 8.0 to ca. 8.5 when mixed in a 1:1 ratio and therefore remained within a suitable range for SAM formation. A time trace is shown below in **Figure 16** that represents fluorescence bursts in a $\approx 1.4 \mu\text{m}^2$ region of the sample in which a nanoparticle resided. The MUAM:TAMRA ratio here was 3:1, the concentration was 100 nM and the acquisition rate was 300 ms.

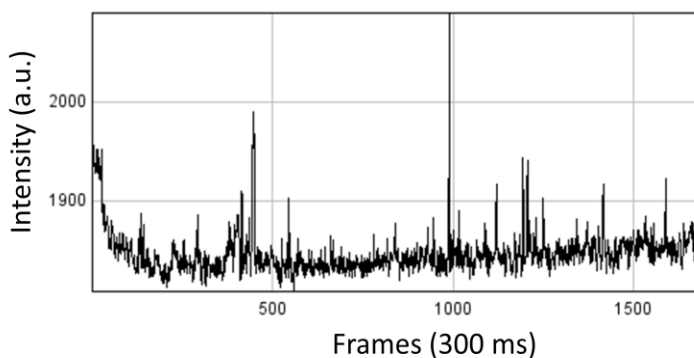


Figure 18. Plasmon enhanced fluorescence imaged as a dye-functionalized SAM molecule formed on the Au nanorod surface from 3:1 ethanol to DMSO solution.

A time-trace of fluorescence data is shown in **Figure 18**. Data was taken for 1875 frames in this case with an acquisition time of 300 ms. This makes the total actual time of the data collection about 9 minutes. The periodic intensity spikes indicate fluorescence events from the dye-functionalized SAM. Peaks such as the one near the 1000th frame *may* originate from plasmon enhanced fluorescence as the intensity is many times that of the other peaks.

Due to the low probability of 100 % reaction completion between MUAM and TAMRA it is likely that non-functionalized SAM molecules were present in this solution. The nanoparticle surface coverage includes both dye-modified and unmodified MUAM molecules as these species are extremely difficult to separate. The total and relative amounts of each molecule on the surface is unclear, but was roughly approximated from the concentrations of MUAM and TAMRA reactants and probability of dye-functionalized SAM formation. We estimate the surface coverage of AuNRs in ratio of pure MUAM to TAMRA-MUAM to be in the range of ca. 10:1 to 2:1. The uncertainty is due to uncertainties in MUAM and TAMRA concentration (solubility), percentage of product formed, and relative affinity for the Au nanosurface. The rhodamine based, dye functionalized SAM molecules used here contain a large heterocyclic fluorone system which may inhibit monolayer formation or undergo nonspecific binding. Based on the

low concentration, frequency of observed fluorescence and our temporal resolution we find it unlikely that the maximum number of molecules that the Au surface can support formed on the nanoparticle. For this experiment formation of a full surface monolayer is not necessary as long as fluorescent-SAM dynamics occur at a rate fast enough for reasonable data collection time and good signal to noise ratio. We have succeeded in optimizing the parameters suitable for imaging plasmon enhanced fluorescence from dye-functionalized SAM molecules during monolayer formation on Au nanorod surfaces.

Chapter 5: Conclusion and Future Work

5.1 CONCLUSION

The body of work in this thesis described scattering studies of plasmonic noble metal single nanoparticles. Particles were synthesized using a seeded growth technique and their optical properties measured by UV-Vis and LSPR spectroscopies. We imaged plasmon scattering from Ag nanoprisms and Au nanorods using dark field microscopy and recorded the LSPR spectra using a liquid crystal tunable filter and CCD camera. The nanoparticles were exposed to different external dielectrics and the induced spectral shifts in the LSPR wavelength maxima were detected and analyzed with MATLAB code.

Ag nanoprisms were deposited in SiO₂ insulation and a potential was applied across the layer. We found that as a bias was switched on and off the LSPR shifted by a measurable, yet varying amount. Some particles displayed irreversible blue shifting while others displayed reversible red shifting. We concluded that local variations in the embedding SiO₂ structure were likely created by the high voltage applications. These variations led to variations in the local charge and current density which were mainly responsible for the observed behavior. The SAM formation of an alkanethiol molecule on Au nanorods was detected by a shift in the LSPR spectra. Based on our control experiments we concluded that O₂ plasma treatment of Au nanorods has no effect on the location of the LSPR taken in N₂, but caused five times as much red shift compared to the shift of untreated particles after incubation in solution. Also, the incubation of Au nanorods in solvent only caused a spectral shift when the N₂ drying step was included. We found that the introduction of a monolayer to the nanoparticle surface resulted in a moderate red shift in the plasmon resonance. The reason the magnitude of the shift was less than expected may have been due to incomplete SAM formation. The same alkanethiol molecules were then functionalized with a fluorescent dye and used to form a

SAM on Au nanorods. The reaction of alkanethiol and dye molecules was confirmed with solid GRAS IR. Plasmon enhanced fluorescence was observed as the dye-functionalized SAMs formed from solution on the Au surface. The conditions of this experiment were optimized with respect to the dye and SAM molecule reaction conditions, solvent type, dye-functionalized SAM solution and optical settings. We concluded that a ratio of 1:1 – 3:1 SAM molecules to dye molecules, a 100 nM concentration and a 100 ms – 300 ms acquisition rate gave the best imaging conditions in terms of signal-to-noise.

5.2 FUTURE WORK

The SAM control experiments were motivated as a precursor to a plasmon enhanced fluorescence study currently being developed. The primary goal of the study is to obtain structural information from Au nanorods, but the technique can be extended to study other plasmonic nanoparticles. The shape and size of a plasmonic nanoparticle can be constructed by imaging the formation of fluorescent SAM molecules on the particle surface. Under optimized conditions fluorescence from the modified SAM which has been enhanced by the plasmonic nanoparticle will be optically distinguishable from unenhanced fluorescence. Fluorescence imaged as diffraction limited spots can then be processed by point spread function (PSF) fitting to a two-dimensional Gaussian function. This powerful technique can be used to approximate the origin of a diffraction limited point source to within at least ca. 20 % error.⁴³ This non-destructive, single nanoparticle characterization technique can provide information about the crucial relationship between plasmonic nanoparticle structure and EM field enhancement. This has enormous implications as the EM field enhancement is the phenomenon responsible for such powerful and sensitive plasmonic applications.

References

1. McLintock, A.; Hunt, N.; Wark, A. W., Controlled side-by-side assembly of gold nanorods and dye molecules into polymer-wrapped SERRS-active clusters. *Chemical Communications* 47, (13), 3757-3759.
2. Nam, J.; Won, N.; Jin, H.; Chung, H.; Kim, S., pH-Induced Aggregation of Gold Nanoparticles for Photothermal Cancer Therapy. *Journal of the American Chemical Society* 2009, 131, (38), 13639-13645.
3. Tian, Y.; Tatsuma, T., Mechanisms and applications of plasmon-induced charge separation at TiO₂ films loaded with gold nanoparticles. *Journal of the American Chemical Society* 2005, 127, (20), 7632-7637.
4. Wurtz, G. A.; Evans, P. R.; Hendren, W.; Atkinson, R.; Dickson, W.; Pollard, R. J.; Zayats, A. V.; Harrison, W.; Bower, C., Molecular plasmonics with tunable exciton-plasmon coupling strength in J-aggregate hybridized Au nanorod assemblies. *Nano Letters* 2007, 7, (5), 1297-1303.
5. Kelly, K. L.; Coronado, E.; Zhao, L. L.; Schatz, G. C., The optical properties of metal nanoparticles: The influence of size, shape, and dielectric environment. *Journal of Physical Chemistry B* 2003, 107, (3), 668-677.
6. Schatz, G. C.; Young, M. A.; Van Duyne, R. P., Electromagnetic mechanism of SERS. *Surface-Enhanced Raman Scattering: Physics and Applications* 2006, 103, 19-45.
7. Bohren, C. F., Huffman, D. R., *Absorption and Scattering of Light by Small Particles*. Wiley: New York, 1983.
8. Mie, G., Contributions to the optics of turbid media, especially colloidal metal solutions. *Annals of Physics* 1908, 25, 377-445.
9. Anker, J. N.; Hall, W. P.; Lyandres, O.; Shah, N. C.; Zhao, J.; Van Duyne, R. P., Biosensing with plasmonic nanosensors. *Nature Materials* 2008, 7, (6), 442-453.
10. Willets, K. A.; Van Duyne, R. P., Localized surface plasmon resonance spectroscopy and sensing. In *Annual Review of Physical Chemistry*, Annual Reviews: Palo Alto, 2007; Vol. 58, pp 267-297.
11. Zhang, J. Y.; Atay, T.; Nurmikko, A. V., Optical Detection of Brain Cell Activity Using Plasmonic Gold Nanoparticles. *Nano Letters* 2009, 9, (2), 519-524.
12. Hagemann, DESY Report SR-74/7. In Hamburg, 1984.
13. Lee, K. S.; El-Sayed, M. A., Gold and silver nanoparticles in sensing and imaging: Sensitivity of plasmon response to size, shape, and metal composition. *Journal of Physical Chemistry B* 2006, 110, (39), 19220-19225.
14. Jin, R. C.; Cao, Y. C.; Hao, E. C.; Metraux, G. S.; Schatz, G. C.; Mirkin, C. A., Controlling anisotropic nanoparticle growth through plasmon excitation. *Nature* 2003, 425, (6957), 487-490.
15. Raj, C. R.; Okajima, T.; Ohsaka, T., Gold nanoparticle arrays for the voltammetric sensing of dopamine. *Journal of Electroanalytical Chemistry* 2003, 543, (2), 127-133.

16. Haes, A. J.; Zou, S. L.; Schatz, G. C.; Van Duyne, R. P., A nanoscale optical biosensor: The long range distance dependence of the localized surface plasmon resonance of noble metal nanoparticles. *Journal of Physical Chemistry B* 2004, 108, (1), 109-116.
17. Haes, A. J.; Van Duyne, R. P., A nanoscale optical biosensor: Sensitivity and selectivity of an approach based on the localized surface plasmon resonance spectroscopy of triangular silver nanoparticles. *Journal of the American Chemical Society* 2002, 124, (35), 10596-10604.
18. Jung, L. S.; Campbell, C. T.; Chinowsky, T. M.; Mar, M. N.; Yee, S. S., Quantitative interpretation of the response of surface plasmon resonance sensors to adsorbed films. *Langmuir* 1998, 14, (19), 5636-5648.
19. Lipson, S. G., Lipson, H. , *Optical Physics*. 2nd ed.; Cambridge: New York, 1981.
20. Instruments, O. <http://www.oxford-instruments.com/Pages/home.aspx>
21. Haynes, W. M., *Physical Constants of Organic Compounds*. In 92nd ed.; CRC Press/Taylor and Francis: Boca Raton, FL, 2012 (Internet Version).
22. Jin, R. C.; Cao, Y. W.; Mirkin, C. A.; Kelly, K. L.; Schatz, G. C.; Zheng, J. G., Photoinduced conversion of silver nanospheres to nanoprisms. *Science* 2001, 294, (5548), 1901-1903.
23. Townsend, P. D., OPTICAL EFFECTS OF ION-IMPLANTATION. *Reports on Progress in Physics* 1987, 50, (5), 501-558.
24. Yanase, A.; Komiyama, H., INSITU OPTICAL OBSERVATION OF OXYGEN-ADSORPTION-INDUCED REVERSIBLE CHANGE IN THE SHAPE OF SMALL SUPPORTED SILVER PARTICLES. *Surface Science* 1992, 264, (1-2), 147-156.
25. Hosono, H., SIMPLE CRITERION ON COLLOID FORMATION IN SIO₂ GLASSES BY ION-IMPLANTATION. *Japanese Journal of Applied Physics Part 1- Regular Papers Short Notes & Review Papers* 1993, 32, (9A), 3892-3894.
26. Malinsky, M. D.; Kelly, K. L.; Schatz, G. C.; Van Duyne, R. P., Chain length dependence and sensing capabilities of the localized surface plasmon resonance of silver nanoparticles chemically modified with alkanethiol self-assembled monolayers. *Journal of the American Chemical Society* 2001, 123, (7), 1471-1482.
27. Hubenthal, F.; Vogel, F.; Trager, F., Fluence dependence of the tailoring of colloidal gold particles with nanosecond-pulsed laser light. In *Synthesis and Photonics of Nanoscale Materials VII*, Dubowski, J. J.; Geohegan, D. B.; Trager, F., Eds. *Spie-Int Soc Optical Engineering*: Bellingham, Vol. 7586.
28. Fleming, M. S.; Walt, D. R., Stability and exchange studies of alkanethiol monolayers on gold-nanoparticle-coated silica microspheres. *Langmuir* 2001, 17, (16), 4836-4843.
29. Park, J. J.; Lacerda, S.; Stanley, S. K.; Vogel, B. M.; Kim, S.; Douglas, J. F.; Raghavan, D.; Karim, A., Langmuir Adsorption Study of the Interaction of CdSe/ZnS Quantum Dots with Model Substrates: Influence of Substrate Surface Chemistry and pH. *Langmuir* 2009, 25, (1), 443-450.

30. Zhang, S.; Huang, F.; Liu, B. H.; Ding, J. J.; Xu, X.; Kong, J. L., A sensitive impedance immunosensor based on functionalized gold nanoparticle-protein composite films for probing apolipoprotein A-I. *Talanta* 2007, 71, (2), 874-881.
31. Chen, H. J.; Kou, X. S.; Yang, Z.; Ni, W. H.; Wang, J. F., Shape- and size-dependent refractive index sensitivity of gold nanoparticles. *Langmuir* 2008, 24, (10), 5233-5237.
32. Mayer, K. M.; Lee, S.; Liao, H.; Rostro, B. C.; Fuentes, A.; Scully, P. T.; Nehl, C. L.; Hafner, J. H., A label-free immunoassay based upon localized surface plasmon resonance of gold nanorods. *ACS Nano* 2008, 2, (4), 687-692.
33. Huang, X. H.; El-Sayed, I. H.; Qian, W.; El-Sayed, M. A., Cancer cell imaging and photothermal therapy in the near-infrared region by using gold nanorods. *Journal of the American Chemical Society* 2006, 128, (6), 2115-2120.
34. Chandrasekar, G.; Mougin, K.; Haidara, H.; Vidal, L.; Gnecco, E., Shape and size transformation of gold nanorods (GNRs) via oxidation process: A reverse growth mechanism. *Applied Surface Science* 257, (9), 4175-4179.
35. Brockman, J. M.; Frutos, A. G.; Corn, R. M., A multistep chemical modification procedure to create DNA arrays on gold surfaces for the study of protein-DNA interactions with surface plasmon resonance imaging. *Journal of the American Chemical Society* 1999, 121, (35), 8044-8051.
36. Smith, E. A.; Wanat, M. J.; Cheng, Y. F.; Barreira, S. V. P.; Frutos, A. G.; Corn, R. M., Formation, spectroscopic characterization, and application of sulfhydryl-terminated alkanethiol monolayers for the chemical attachment of DNA onto gold surfaces. *Langmuir* 2001, 17, (8), 2502-2507.
37. Wallwork, M. L.; Smith, D. A.; Zhang, J.; Kirkham, J.; Robinson, C., Complex chemical force titration behavior of amine-terminated self-assembled monolayers. *Langmuir* 2001, 17, (4), 1126-1131.
38. Stamboliyska, B. A.; Binev, Y. I.; Radomirska, V. B.; Tsenov, J. A.; Juchnovski, I. N., IR spectra and structure of 2,5-pyrrolidinedione (succinimide) and of its nitranion: experimental and ab initio MO studies. *Journal of Molecular Structure* 2000, 516, (2-3), 237-245.
39. Frutos, A. G.; Brockman, J. M.; Corn, R. M., Reversible protection and reactive patterning of amine- and hydroxyl-terminated self-assembled monolayers on gold surfaces for the fabrication of biopolymer arrays. *Langmuir* 2000, 16, (5), 2192-2197.
40. Kinugasa, S. T., K.; Tamura, T., Spectral Database for Organic Compounds (SDBS). In Tsukuba Advanced Computing Center (TACC): National Institution of Advanced Industrial Science and Technology.
41. Brauer, C. S.; Craddock, M. B.; Kilian, J.; Grumstrup, E. M.; Orilall, M. C.; Mo, Y. R.; Gao, J. L.; Leopold, K. R., Amine-hydrogen halide complexes: Experimental electric dipole moments and a theoretical decomposition of dipole moments and binding energies. *Journal of Physical Chemistry A* 2006, 110, (33), 10025-10034.
42. Sen, T.; Patra, A., Resonance energy transfer from rhodamine 6G to gold nanoparticles by steady-state and time-resolved spectroscopy. *Journal of Physical Chemistry C* 2008, 112, (9), 3216-3222.

43. Stranahan, S. M.; Willets, K. A., Super-resolution Optical Imaging of Single-Molecule SERS Hot Spots. *Nano Letters* 2011, 10, (9), 3777-3784.